LAWRENCE
LIVERMORE
NATIONAL
LABORATORY

UCRL-JRNL-215446

As-Built Modeling of Ojbects for Performance Assessment

E. J. Kokko, H. E. Martz, D. J. Chinn, H. R. Childs, J. A. Jackson, D. H. Chambers, D. J. Schneberk, G. A. Clark

September 16, 2005

Journal of Computing and Information Science in Engineering

As-Built Modeling of Objects for Performance Assessment

Edwin J. Kokko, Harry E. Martz, Jr., Diane J. Chinn, Henry R. Childs, Jessie A. Jackson, David H. Chambers, Daniel J. Schneberk, and Grace A. Clark
Lawrence Livermore National Laboratory, 7000 East Avenue, Livermore, CA, 94550

Article submitted to special issue of JCISE on 3D Computational Metrology, Reverse Engineering, and emerging scanning technologies (Original: September 22nd 2005, Revised: March 17 2006, Accepted: June 6th 2006).

Keywords: as-built modeling, model-based engineering, reverse engineering, finite element analysis, non-destructive characterization, X-ray digital radiography, X-ray computed tomography, ultrasonics, data fusion, visualization

1 Abstract

The goal of "as-built" computational modeling is to incorporate the most representative geometry and material information for an (fabricated or legacy) object into simulations. While most engineering finite element simulations are based on an object's idealized "as-designed" configuration with information obtained from technical drawings or computer-aided design models, "as-built" modeling uses nondestructive characterization and metrology techniques to provide the feature information. By incorporating more representative geometry and material features as initial conditions, the uncertainty in the simulation results can be reduced, providing a more realistic understanding of the event and object being modeled.

In this paper, key steps and technology areas in the as-built modeling framework are: (1) inspection using non-destructive characterization (NDC) and metrology techniques; (2) data reduction (signal and image processing including artifact removal, data sensor fusion, and geometric feature extraction); and (3) engineering and physics analysis using finite element codes. We illustrate the process with a cylindrical phantom and include a discussion of the key concepts and areas that need improvement. Our results show that reasonable as-built initial conditions based on a volume overlap criteria can be achieved and that notable differences between simulations of the as-built and as-designed configurations can be observed for a given load case. Specifically, a volume averaged difference of accumulated plastic strain of 3% and local spatially varying differences up to 10%. The example presented provides motivation and justification to engineering teams for the additional effort required in the as-built modeling of high value parts. Further validation of the approach has been proposed as future work.

2 Introduction

In practice, most engineering finite element analysis models[1] are based on an object's idealized "as-designed" configuration with information obtained from technical drawings and computer aided-design models. Lawrence Livermore National Laboratory (LLNL) has been using engineering and physics computational analysis codes to assess the performance of objects in the "as-built" configuration. As-built features might include geometry deviations (asymmetries, dents, etc) or material anisotropies and flaws (inclusions, voids, cracks, delamination, ablation regions, etc) originating from the manufacturing process or from the object being exposed to or aged in a certain physical environment during service conditions. The objective is to enable engineers and physicists to build (finite element) analysis models using more accurate initial conditions (geometry and material features) obtained from non-destructive methods. With more realistic initial conditions, the numerical models have the potential to provide new insight into the performance of an object or experiment.

The idea of as-built modeling is not new and has many of the same concepts of reverse engineering and model-based engineering. Applications of industrial as-built modeling at LLNL and elsewhere vary from capturing and analyzing casting [1,2] and welding defects [3,4], through modeling the mechanical response of complex polymer foam structures [5 - 6] and woven composite materials [7], to analyzing automotive components [8,9] including engines [10]. Industrial applications typically use as-

[1] The term "analysis model" is used in a general context and can be loosely defined as any computational model constructed and used as input to a numerical analysis code (finite element, finite volume, multi-body dynamics, etc) requiring some geometric (2-D or 3-D) and material detail in order to capture a certain class of physics (mechanical, thermal, electrical, electro-magnetic, etc.).

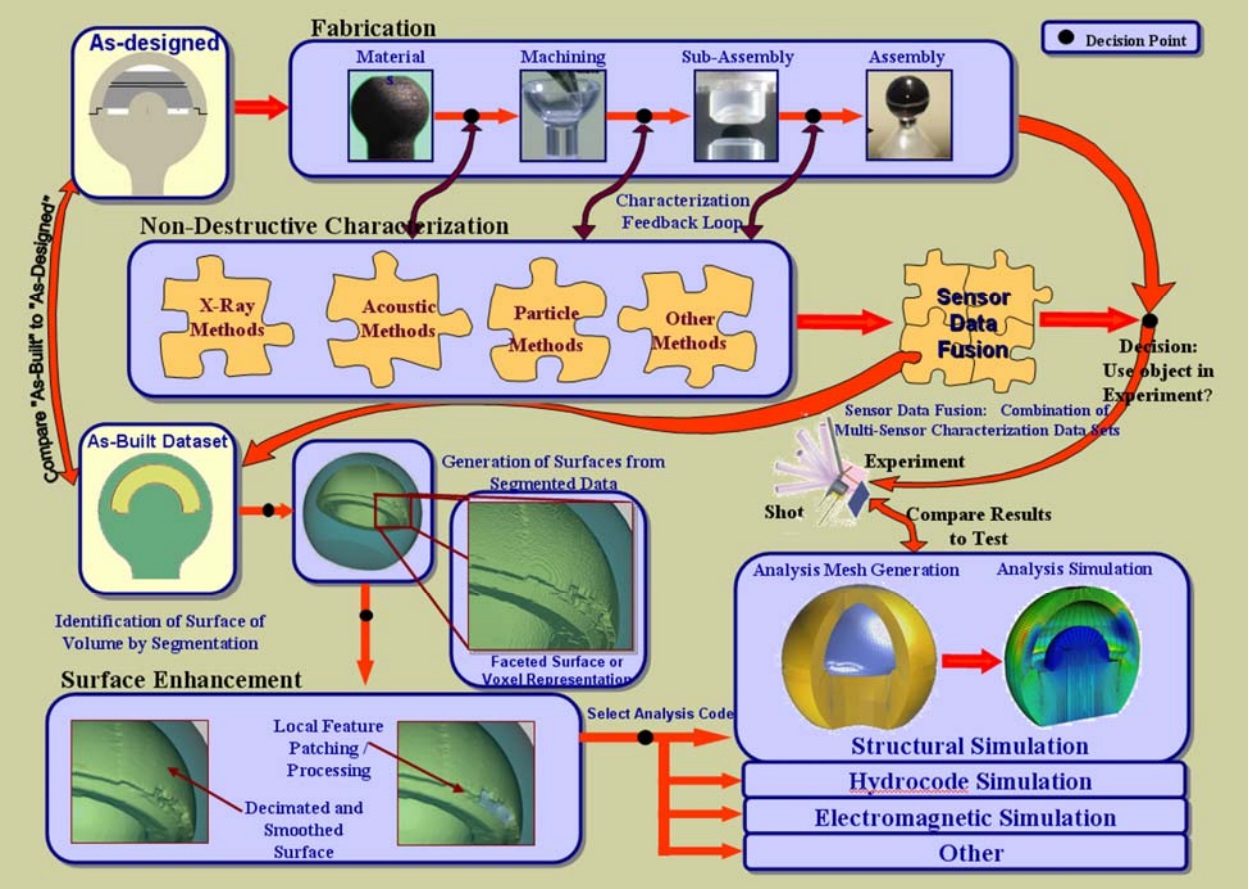

Figure 1: Example as-built modeling process applied to a spherical reference standard.

designed information in place of as-built data for simulations; the medical field has no such data. Current "patient-specific" medical applications span all areas of medicine, including: human bones and orthopedic implant evaluation [11 - 15]; detailed sub-scale trabecular bone research and modeling [16,17]; cardiovascular system flow modeling [18, 19]; and the modeling of cancerous tumors [20].

A single as-built modeling approach does not necessarily work for every analysis scenario especially for the diverse range of industrial applications. However, each approach has several common steps (summarized in Figure 1): (1) inspection using non-destructive characterization (NDC) and metrology techniques; (2) data reduction (signal and image processing including artifact removal, data sensor fusion, and geometric feature extraction); and (3) engineering and physics analysis using computational analysis codes. NDC data can be used to create an as-built model for seeding engineering and physics simulation initial conditions to analyze and determine whether this object should be used in an experiment or test, as well as providing insight and comparison to the empirical results of the test. We illustrate the process with a cylindrical phantom and include a discussion of the key concepts and areas that need improvement. Comparison of as-built to as-designed model simulations shows that there can be notable differences in results.

3 Data Conditioning

In our research, development and reduction–to–practice efforts, we are focusing on driving the as-built modeling process from the end goal of numerical analysis (i.e. the analyst point of view). One of the challenges is determining how to condition the data for the class of physics simulation, the goals of the simulation, and the modeling assumptions that will be used. A simplified approach was adopted where each analysis problem is assumed to fit into one of four types that address modeling issues from geometry and material complexities (as summarized in Table 1).

		Material	
		Simple	Complex
Geometry	Simple	Type I	Type II
	Complex	Type III	Type IV

Table 1: Schematic showing the different data conditions used in classifying NDC data sets. Each type has differing levels of difficulty in generating the mesh for an as-built object model.

3.1 Simple Versus Complex

Our approach groups geometry and material modeling techniques based on information that is included in the analysis simulation. Taking a "simple" modeling approach either implies one of two things. Either that the object geometry and material regions are very structured (simple shapes and homogeneous) or that inherently complex details (material and geometry) are being artificially simplified or omitted as a modeling assumption for the simulation. Conversely, a "complex" modeling approach omits very little detail and preserves material and geometry details across multiple scales.

For example, consider the object detailed in Figure 1. For this scenario the analyst building the finite element analysis model decided that the complex geometry asymmetries (dents / pockets) were important to capture but assumed any material inhomogenities were negligible to the object response. This approach would fall into a Type III analysis. After simulating the object, the analyst may retract the simplified material modeling approach and decide to include more material region detail. The analysis would then fall into a Type IV modeling approach allowing for graded material properties to be modeled as well as direct, discrete material property mapping (from an NDC data set) in each material region. In the future, these coarse groupings are intended to speed the selection of algorithms for data conditioning and mesh generation for cases that have been proven to work for the level of detail required by the analyst. This is the first step toward semi-automating the as-built modeling process.

4 Process Illustration

In order to illustrate some of the issues associated with as-built modeling, three simple phantoms were designed and manufactured. The intention of using a simple phantom is to easily highlight the differences that exist between an idealized "designed" object and the physical as-built product (in the general sense) and that modeling in the as-built configuration presents new challenges at every level. Design, fabrication, NDC, data reduction and simulation/analysis illustrates one exemplar as-built modeling process and current limitations in the process where further research is required. A schematic of the process described in this paper is shown in Figure 2. The phantom data sets were used to exercise software algorithms and the process used as well as will serve as a technical discussion perspective, while keeping the application simple and generic.

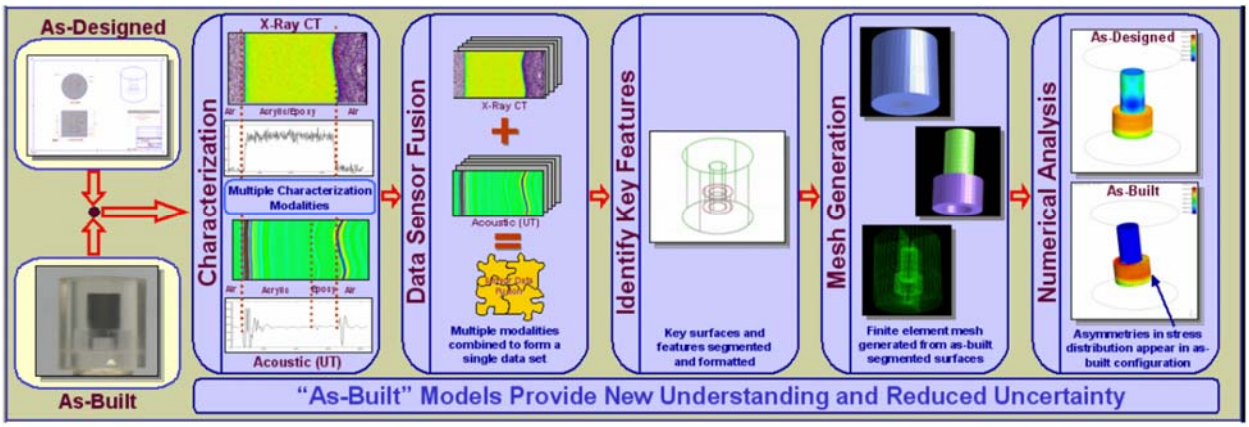

Figure 2: Schematic of the as-built modeling analysis process applied to a concentric cylindrical phantom.

4.1 Design and Fabrication of Three Cylindrical Phantoms

Three phantoms were designed with input from the entire team to facilitate fabrication, inspection, segmentation, meshing and simulation. A Computer Aided Design (CAD) model and photographs of the three phantoms are shown in Figure 3 and 4, respectively. For simplicity, the concentric-cylindrical phantom is highlighted for discussion. The geometric detail for the concentric-cylindrical phantom can be found in Figure 5.

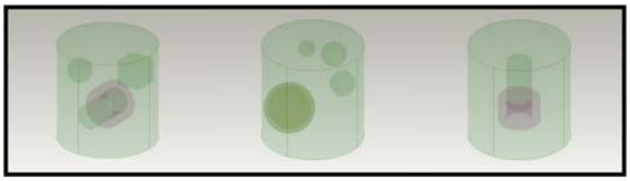

Figure 3: CAD models of the three cylindrical phantoms. This represents the as-designed configuration for each of the objects. As shown, the designs include different geometric features.

Figure 4: Photograph of the three phantoms fabricated. As-built process is discussed for the concentric-cylindrical phantom (on the right).

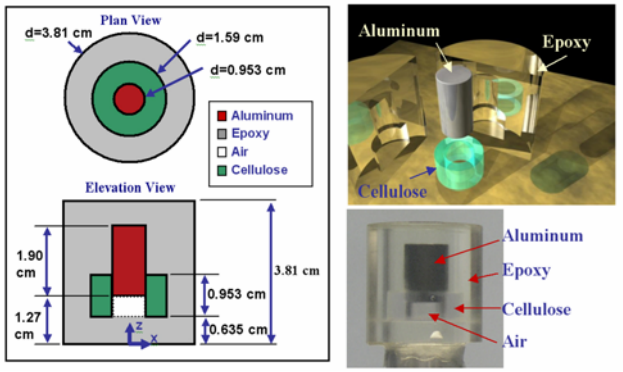

Figure 5: Design details for the concentric-cylindrical phantom (left). Artist's rendering of the designed phantom (top right). Photograph of the as-built phantom (bottom right).

The concentric cylindrical-phantom was manufactured in stages. First, a 0.635–cm layer of epoxy was poured into a cylindrical mold and allowed to set. While the epoxy was setting, the aluminum rod and the cellulose ring were glued together. The resulting aluminum–cellulose composite subassembly was then glued to the hardened epoxy layer. By doing this, an air gap was created within the cellulose ring below the aluminum rod. Finally, the remaining epoxy was poured over the composite aluminum-cellulose-air components.

4.2 Non-Destructive Characterization Systems

The objective of using NDC techniques can vary from attempting to detect and characterize discontinuities (surface or internal), to trying to obtain dimensional and metrology information, to working toward extracting physical properties (elastic and thermal constants, electro-magnetic properties, etc.). NDC modalities available include: X-ray, particle (proton and neutron), sonic and ultrasonic, thermal, surface (dye penetrant and magnetic particle), and mechanical and optical methods. X-ray Computed Tomography (X-ray CT) and Ultrasounic Testing (UT) are the two modalities used here to demonstrate the utility of as-built modeling.

4.2.1 X-ray CT

The digital radiography and computed tomography system called PCAT (see Figure 6) was used to acquire X-ray digital radiographs (or projections) of the concentric-cylindrical phantom. The projections were acquired using a Philips X-ray source with a 1-mm spot size, 200 kV and 5 mA. The X-rays are converted to optical light using a 6–mm thick TbO_2 doped scintillating glass plate. The light emanating from the scintillator is captured by a 200–mm Micro–Nikkor lens coupled to a 14–bit 1–k x 1–k Apogee CCD Camera. 360 projections over 360° in θ and 896 slices along the z-axis were acquired with a 48–µm x 48–µm effective pixel size at the object. A representative X-ray projection is shown in Figure 7 (left).

Figure 6: Photograph of the PCAT digital radiography and computed tomography system (left). Photograph of the inside of the PCAT detector box (right).

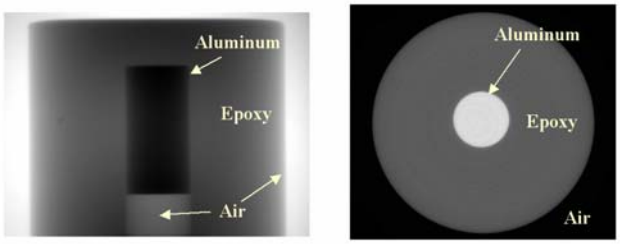

Figure 7: Representative digital radiographic projection, I, (left) and CT slice, μ. (right) of the concentric cylindrical phantom. The projection reveals the epoxy, aluminum rod, and air but not the cellulose. The CT slice is at a location that reveals the epoxy and aluminum materials.

4.2.2 Ultrasound

A full 3D ultrasonic data set was collected on the concentric-cylindrical phantom using pulse-echo immersion testing. The experimental configuration is shown in Figure 8. In pulse-echo testing, a transducer sends an ultrasonic wave into the object. Reflections from interfaces or defects in the object are received by the same transducer. Using a 5–MHz, 12.7–mm diameter, 50.8–mm focal length focused transducer, the cylindrical part is rotated about the θ-axis and indexed along the elevation or z-axis. The transducer sends ultrasonic waves radially into the object with the focus point of the transducer experimentally placed at the epoxy-aluminum interface.

Waveforms, or A-scans, are collected at each UT scan position. The UT scan consists of 360 angles over 360° in θ and 68 positions in z. Scan increments for the data set are $\Delta\theta$ = 1º and Δz = 0.5–mm. The waveforms are digitized at 50–MHz and captured over 20–μs with t_0 = 35.5–μs (see Figure 9). The front surface reflection from the epoxy/water interface occurs at t = 36.3–μs.

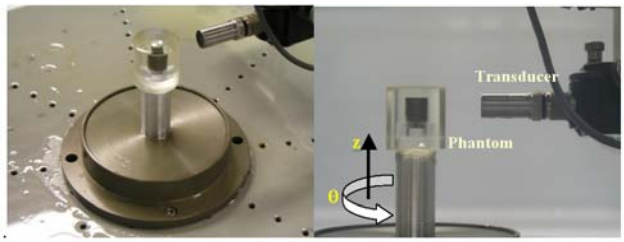

Figure 8: Concentric-cylindrical phantom on ultrasound test bed.

4.3 Data and Image Processing

The image-processing steps were broken down into functional categories, including: artifact removal, image reconstruction, sensor fusion (or data integration), segmentation, and geometric feature extraction / geometric de-featuring. Each category of operations enriches, separates, simplifies, or conditions the data set into a form that can eventually be used by analysis code pre-processors (i.e., mesh generation utilities). The finite element modeling requirements and assumptions were established before processing began.

4.3.1 X-ray CT Data Processing

The following steps were used to process and reconstruct the X-ray radiographic projections into CT images (also known as cross sectional slices or tomograms). First the CCD camera dark current, D, is subtracted from the transmitted, I, and incident irradiance, I_o, X-ray projections. Next the transmitted X-ray projections, I, are normalized from projection to projection, divided by the incident irradiance projection, I_o, then convert to the attenuation image, $\mu\ell$, by taking minus the natural logarithm

$$-\ln\left(\frac{(I-D)}{(I_0-D)}\right)=\mu\ell. \qquad (1)$$

Here μ is the X-ray linear attenuation coefficient and ℓ is the integral path length through a homogeneous material [21]. From all 360 projections a single row is extracted and converted to a sinogram (x vs θ) [22]. This data is further processed to remove pixel outliers, detector-to-detector imbalances and normalized to constant attenuation per projection angle. Each of the 896 sinograms were reconstructed by a convolution back projection algorithm into a 2D tomogram with a volume element (voxel) size of 48–μm x 48–μm x 48–μm (see Figure 7 right). These 2D tomograms are combined into a 3D data array and can be computationally sectioned accordingly.

4.3.2 UT Data Processing

Ultrasonic images can be generated from A-scans. A two-dimensional slice of the phantom, or B-scan image, can be reconstructed by assigning color scale values to amplitude values and plotting waveforms at a given elevation in an image. Figure 9 (bottom) shows a B-scan image of the phantom.

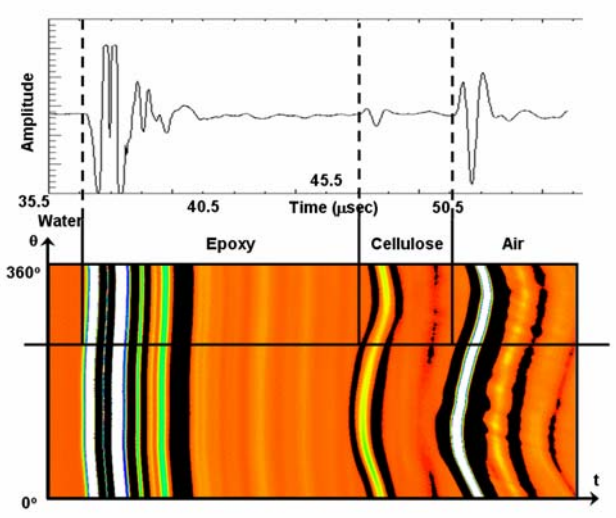

Figure 9: A typical UT waveform or A-scan (top) shows amplitude vs. time of the acoustic signal. A B-scan (bottom) plots multiple A-scans taken by scanning 360º around the object. Amplitude is mapped to color in the B-scan.

4.3.3 X-ray CT and UT Results and Data Fusion

Using multiple methods to characterize the concentric-cylindrical phantom provided additional insight into geometric details since each characterization technique generated a unique and independent object response (i.e. modality-dependent strengths and weaknesses). In particular, the X-ray CT image of the concentric-cylindrical phantom depicted in Figure 10 captures the aluminum-air, aluminum-epoxy, and cellulose-air interfaces but misses the epoxy-cellulose interface. The ultrasonic data set provides some of the missing geometry information by defining the epoxy-cellulose interface, as shown in Figure 10.

The biggest challenge to fusion of different characterization techniques is co-registration of the data sets. For the concentric-cylindrical phantom, we used a manual geometric feature integration procedure (fusion) to combine information from the X-ray CT and UT data sets. The four major steps in fusing the data sets are shown schematically in Figure 11. Each step either aligns or scales the data sets in the r, θ or z-axes. In the first step, the data sets are aligned in z. This is done by finding the slice from each data set that corresponds to the bottom of the phantom. In the next step, the data sets are scaled in the z-axis. The vertical spatial resolution of the CT data (0.048–mm) is much better than the UT data (0.50–mm) so scaling occurs by decimation of the CT data. Sixty-eight CT slices are selected that correspond to the 68 available UT slices, these aligned slices are renumbered and referred to as UT/CT slices.

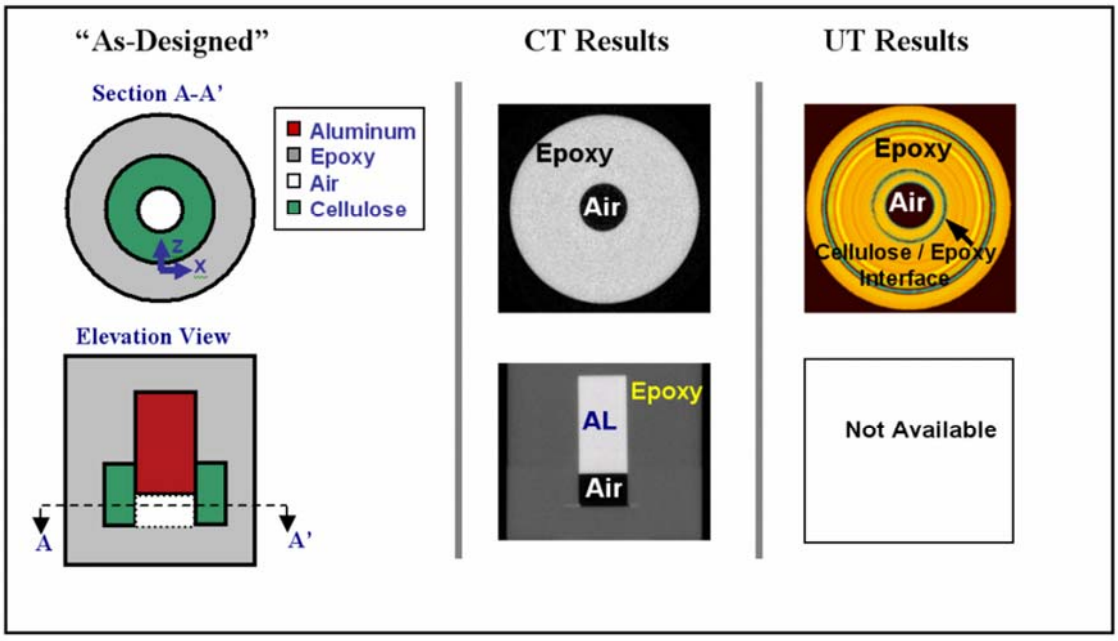

Figure 10: As-designed sketch of section and elevation views (left), CT slice at A-A' (middle-top) and ultrasound slice at A-A' (right-top). Note that section A-A' is located where there is epoxy, cellulose and air. An elevation view from the X-ray CT data is shown at middle-bottom. The CT results clearly reveal the epoxy, aluminum and air but not the cellulose. This is because the X-ray attenuation for cellulose and epoxy are about the same value. The ultrasound slice reveals the epoxy-cellulose interface as indicated.

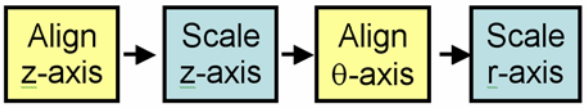

Figure 11: The geometric feature integration procedure (registration) consists of alignment and scaling in each of the axes to obtain consistent spatial coordinates.

When each data set was acquired the rotational starting point on the phantom was not the same. Therefore, the next step in processing is to align the data sets rotationally. This operation is best performed in polar coordinates (r, θ). The polar coordinate images of these slices for the both CT and UT, along with a representative lineout are shown in the Figures 12 and 13. Because the cellulose and aluminum cylinders are not centered in the epoxy, their edges make a distinctive s-curve through the polar CT and UT images (see Figure 12). By manually examining the CT and UT data for one slice it is determined how many UT A-scans would need to be shifted to rotationally align the data sets. The aligned results of two representative slices are shown in Figures 12 and 13. UT/CT slice 20 contains epoxy, cellulose and air, while UT/CT slice 40 contains only epoxy and aluminum.

The final step in co-registering the data sets is scaling in r. UT data is collected temporally while CT data is collected spatially. For single material objects, a single acoustic velocity scale factor can be applied to the UT data to scale it to CT data. On multi-material objects, UT data must be scaled by the acoustic velocity in each material in order to convert to spatial dimensions. Each material and its material specific velocity in the UT data set were scaled using the CT spatial information.

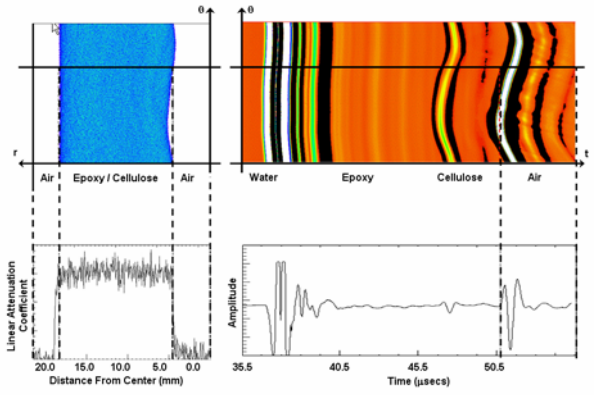

Figure 12: UT/CT Slice 20 X-ray CT polar plot (top left) and lineout (bottom left); ultrasound B-scan (top right) and A-scan (bottom right).

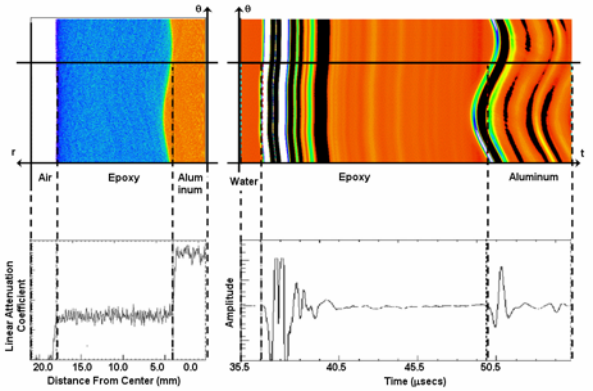

Figure 13: UT/CT Slice 40 X-ray CT polar plot (top left) and lineout (bottom left); ultrasound B-scan (top right) and A-scan (bottom right).

The alignment and scaling process is very time-consuming. This process could be simplified with the judicious use of fiducial markers. However, for many components of interest, fiducial markers are not an option due to the nature of the object. A summary and motivation for integrating the geometry features is in Figure 14.

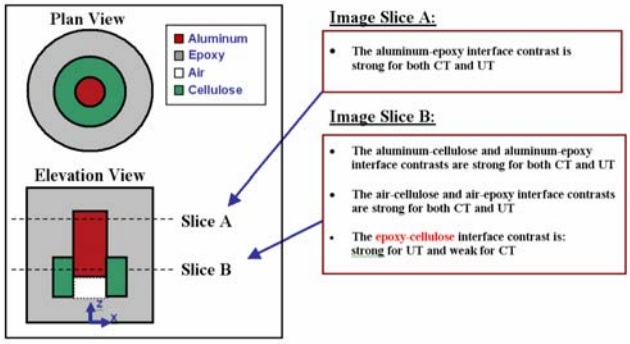

Figure 14: Summary of the CT and UT characterization results.

4.3.4 Using VisIt to View and Extract Geometric Features

When extracting geometric features of interest, careful attention must be paid to analysis code pre-processor requirements and any self-imposed simplifying assumptions made by the analyst. For the concentric–cylindrical phantom example, the asymmetries in the phantom's geometry were of interest and any material property variation (in the form of voids, inclusions, or elastic property gradients) was secondary. This particular analysis fits into the Type III category discussed in Section 3.

When obtained from metrology or NDC, the as-built geometry contains more features and information (small fillets, textured surfaces, etc) than mesh generators can handle or that the analyst wants to include in the finite element analysis calculation [23]. For ill–conditioned geometries, the geometry must be modified or re-conditioned to remove anomalous or problematic features, such as artifacts from NDC methods and noise. All of which cause problems with mesh generator projection algorithms, solid geometry kernels, and potentially within the analysis code. For example, the object depicted in (Figure 1 lower left) had a large aspect ratio cone shaped feature extending from the outside surface into the center volume. The sharp geometric discontinuity was recognized as a potential problem area both when using the mesh generator to discretize the volume and when running the analysis code. A modified surface approximation (or patch) was created to replace the feature with a close representation of the original surface and was noted as an approximation.

VisIt was used to visualize, segment and extract geometric features of interest from the concentric-cylindrical phantom CT data set. Developed at LLNL, VisIt is an end-user 3D visualization and data analysis tool intended for interacting with large and diverse data sets in real-time [24]. The tool is fully parallelized with good scalability and can handle single or multiple data sets simultaneously ranging in size from thousands to billions of data points.

Segmenting the geometric features of interest within VisIt was accomplished in multiple steps. In the first step, the high-frequency noise common in CT data was removed by applying a mean filter. Once the data was filtered, the second step was to probe the data and determine the range in X-ray attenuation values identifying each material region. For this example, disjoint X-ray attenuation ranges existed between the aluminum, air, and epoxy regions. However, as previously mentioned, the epoxy and cellulose regions were indistinguishable in X-ray attenuation. A bounding box approach was used to separate the air inside the cellulose ring from the air outside the phantom. The final step was to extract the three volumes: aluminum, the enclosed air, and a manufacturing glue defect region as shown in Figure 15. This was accomplished by using an isovolume algorithm. The algorithm is similar to an isosurface except it creates a volume for all points in space within the data set that fall with a specified X-ray attenuation range.

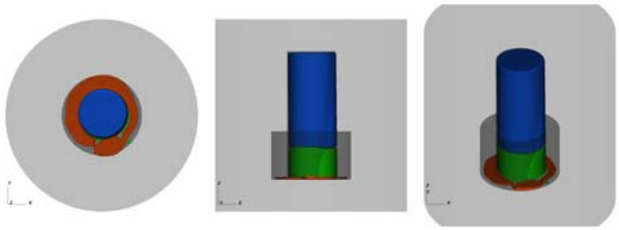

Figure 15: Segmented isovolumes for the as-built geometry. The light–grey represents epoxy, the blue region represents the aluminum, the green region the air pocket, and the orange region a manufacturing feature (glue). These materials were directly determined from the X-ray CT data. Note that the area shaded in dark gray representing the cellulose region was determined from the UT data and manually included for visualization. The cellulose region was not processed directly within VisIt.

Once the X-ray CT data was segmented, several additional operations were necessary in order to extract the geometric features in a form useable by an analysis mesh processor, such as TrueGrid [25] or Cubit [26]. Starting with the volumes calculated in the segmentation phase, the first operation was to define the surface bounding the isovolume. This generated three isosufaces resulting in 899,854 total facets. To obtain a manageable number of surfaces, smoothing and decimation algorithms were applied until the total surface triangle count neared 250,000. Applying these operators removes small surface fluctuations while reducing the number of triangles describing the surface and makes it easier to import and manipulate within the selected mesh generator.

Once the data set had been smoothed and decimated, a 3D Delaunay triangulation operator was applied to the data set to filter out small detailed features in the glue material regions that were identified as potential problem areas for the mesh generator (see Figure 16). Finally, the conditioned surfaces were exported and converted to a file format compatible for import into the selected mesh generation software, in this case a Stereolithography (STL) format for Cubit.

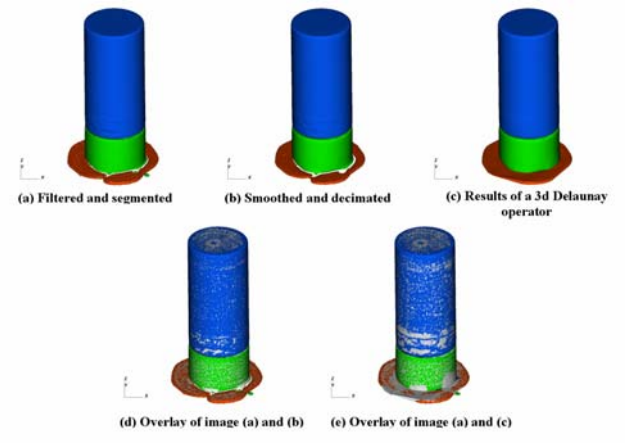

Figure 16: Geometric feature extraction operations for aluminum, air, and glue regions (a) – (c) as labeled. Note that with each operation slight deviations (grey) from the original data accumulate as shown in (d) and (e).

4.3.5 Mesh Generation

At this point, the features isolated from the phantom are used to build a finite element analysis model. Geometric features (such as lines, surfaces, volumes) are imported into mesh generation tools (such as TrueGrid [25] and Cubit [26]) and used as primitives for the physical discretization (or mesh) required by the analysis codes that will be used to simulate different classes of physics. For select analyses, material features of interest that are statistical in nature (for example: density gradients or void size, shape, and spatial distribution) are processed for use in analysis code material models.

The analyst is limited to using mesh generation algorithms tailored to the element types available in the analysis code [23]. Non-linear structural engineering codes generally require that the finite element mesh be limited to hexahedral and quadrilateral element types. Hexahedral meshes typically provide better solutions with fewer required degrees–of–freedom than tetrahedral element meshes [27-28]. Even though there are many approaches to mesh generation, there are limited useful automated methods that produce a valid finite element mesh in three dimensions for a general object [29,30].

In addition, other modeling assumptions imposed by the analyst need to be considered when generating the analysis mesh, specifically, the type of analysis method [Eulerian, Lagrangian, Arbitrary–Lagrange–Eulerian (ALE), Smooth Particle Hydrodynamics (SPH), etc.] and the class of physics to be simulated. Each method has varying degrees of flexibility in the mesh generation step. In a conforming grid, the analysis mesh stays true to the actual geometry preserving all boundaries. Non-conforming grid methods take advantage of semi-automated algorithms to approximate the geometry. A common non-conforming approach, and used in the concentric-cylinder example analysis, is to calculate the volume overlap between the geometry of interest and the elements of a background mesh (typically referred to as “painting” or “shaping” [31]).

For the three extracted volumes (Figure 15), the aluminum, the enclosed air, and glue bounding surfaces were imported into Cubit as STL geometry directly out of Visit. The cellulose bounding surface was manually added into the model using dimensional information obtained from the ultrasound data. Once the geometry was defined within Cubit, it was necessary to add a number of geometric “webcuts” [26] to the geometry description and specify a desired element mesh density to guide the mesh generator. For this particular analysis, a tetrahedral discretization scheme to describe the geometry was deemed acceptable since the material regions would be “shaped” over a background hexahedral grid for subsequent analysis using a non-conforming grid method (more details provided in Section 4.4 Engineering Analysis and Results). Since automatic tetrahedral mesh generation algorithms are relatively robust, no further manipulation or guidance was necessary for the algorithm to generate a mesh. The geometry and geometry mesh applied to the phantom within Cubit is shown in Figure 17.

After the mesh has been generated, boundary conditions are typically specified and applied to the geometry. For this particular analysis, only the physical region discretization was necessary since all necessary boundary conditions would be logically applied within the analysis code itself. Finally, the analysis mesh was exported into a Cubit Genesis/Exodus format file.

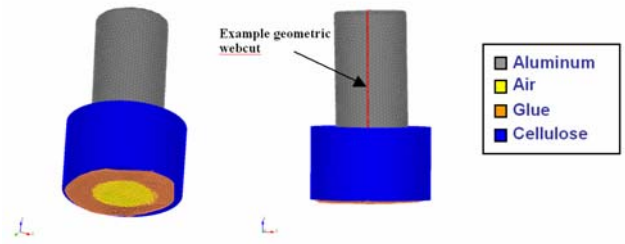

Figure 17: Cubit tetrahedral mesh for describing the as-built geometry from the VisIt STL concentric-cylindrical phantom data set.

4.4 Engineering Analysis and Results

The comparison of the as-designed versus the as-built geometry are shown in Figures 18 thru 20. The as-built object geometry has slightly different features (i.e. glue region) and is slightly rotated in the global coordinate frame. The longitudinal axis of the as-built system was misaligned compared to the as-designed system by less than two degrees about each of the three global axes. This was determined by examining the centroid, moments of inertia, and direction cosines for the as-built assembled system in VisIt (reference Table 3). Table 2 shows the calculated volumes for the as-designed geometry and the as-built configuration as-meshed prior to analysis as well as the percent component volume overlap between the two models. In addition, the approach used to extract the as-built computational model proved to provide reasonable initial geometry conditions when compared to the X-ray CT data based on a volume overlap criteria. Although better metrics exist (refer to future work in section 5 below), a volume overlap correlation of 97.6% was calculated. Given the number of operations in the process, starting with the X-ray CT data through to the final meshed as-built object, this metric provided confidence in the initial accuracy of the as-built model geometry.

The LLNL hydrocode ALE3D [31] was used to apply a sharp pressure load to the top surface (+z surface) of the epoxy portion of the phantom. The model was built by using the shape overlay feature of ALE3D to place the discretized as-built geometry regions (from Cubit) for both the as-designed and as-built geometry over a 1,440,000 hexahedral element epoxy background grid. The motion of the shaped-in object was restricted by a stonewall translation boundary condition applied to the bottom surface (-z surface) of the epoxy. The goal of the example analysis simulation was to observe and quantify any differences in response between the as-designed and as-built concentric-cylindrical phantom models.

The analysis results for the as-built configuration were compared to the as-designed configuration for the same load case. As expected, the results indicate a sensitivity to the asymmetries introduced in the as-built model (as shown in Figures 18-20 and Tables 2 and 3). In the as-designed configuration the pressure load propagates with axial-symmetry through the epoxy matrix and around the components embedded in the epoxy phantom. In the as-built configuration, the simulation begins by looking very similar to the as-designed but later in time the pressure wave is interrupted and perturbed by the misaligned components within the model. Time-sequence pseudocolor plots of pressure and effective plastic-strain for the as-built and as-designed simulations are shown in Figures 21 and 22. A difference plot quantitatively illustrating the spatial and temporal differences in accumulated effective plastic strain between the as-designed and as-built models is provided in Figure 23 and 24. From these results we determined a marked difference of 3% in volume averaged effective plastic strain with local spatially varying differences up to 10%. Such differences could indicate problems in an assembled or aged system that could result in degraded performance or possible failure from unintended stress localizations under the given load case.

Ultimately, it is up to the end-user to determine the added value of performing an as-built analysis. The result of this process illustration was one of the first steps on the way to understanding how to routinely incorporate as-built geometric and material information into analysis models. Programs at LLNL are beginning to leverage this methodology with the goal of improving engineering and physics analysis models, reducing calculation uncertainty and providing better experimental understanding of manufactured and legacy objects as well as determining if the as-built object will meet performance specifications.

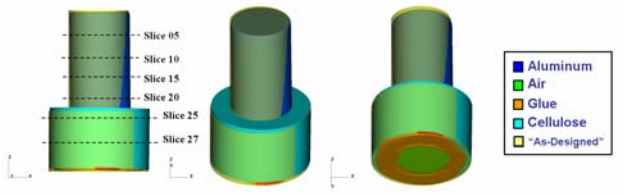

Figure 18: "As-designed" versus "as-built" phantom. The as-built material regions are specified in the key on the right. The baseline as-designed object is represented as a semi-transparent yellow color superimposed over the as-built material regions. Note the model slice numbers shown have no correlation to the NDC slice numbers in previous figures.

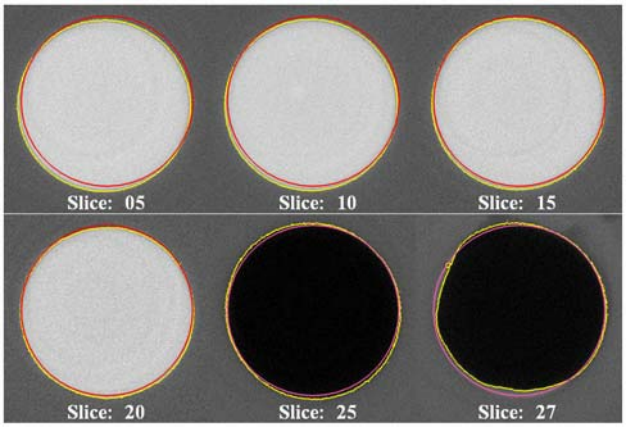

Figure 19: The as-designed geometry (in red) and the as-built geometry geometry (in yellow) are superimposed over the as-built CT results. The location of the slice numbers are shown in Figure 18. Slices 05 through 20 reveal the aluminum while 25 and 27 reveal the air (with the cellulose absent from the data).

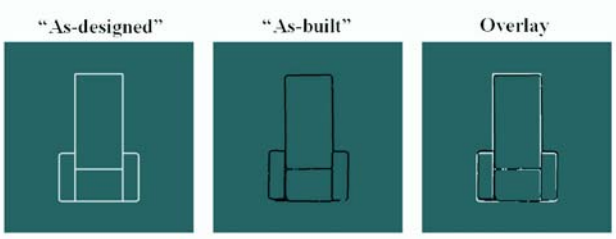

Figure 20: Elevation cross-sections of the as-designed and as-built models. The rightmost figure is an overlay of the as-built on the as-designed.

	As-Built (cm^3)	As-Designed (cm^3)	Overlap (%)
Epoxy	40.42	40.27	99.6%
Cellulose	1.18	1.08	91.5%
Aluminum	1.33	1.25	94.0%
Air	0.41	0.40	97.3%
Glue	0.05	0.00	0.0%

Table 2: Volume overlap and component volume comparison between the as-designed and as-built initial configurations.

	As-Designed Centroids			As-Built Centroids		
	X (cm)	Y (cm)	Z (cm)	X (cm)	Y (cm)	Z (cm)
Cellulose	0.00E+00	0.00E+00	1.11E+00	1.44E-02	1.48E-02	1.15E+00
Aluminum	0.00E+00	0.00E+00	2.22E+00	2.41E-02	3.62E-02	2.21E+00
Air	0.000	0.000	9.52E-01	2.08E-02	1.13E-02	9.56E-01
Glue	N/A	N/A	N/A	-1.20E-01	-7.40E-02	6.64E-01
Total	0.000	0.000	1.59E+01	1.86E-02	2.31E-02	1.59E-01

As-Designed

$$\begin{bmatrix} 47905.8 & 0.0 & 0.0 \\ 0.0 & 47905.8 & 0.0 \\ 0.0 & 0.0 & 15128.2 \end{bmatrix}$$

As-Built

$$\begin{bmatrix} 46692.4 & -4.2 & -334.6 \\ -4.2 & 46714.7 & -303.1 \\ -334.6 & -303.1 & 15334.6 \end{bmatrix}$$

Table 3: As-designed and as-built centroids and moment of inertia tensors.

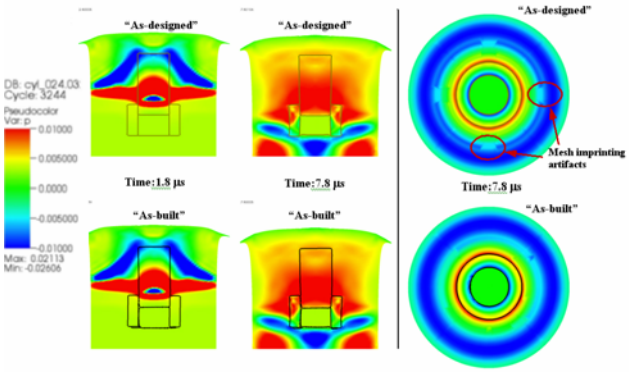

Figure 21: Pressure time-sequence plots for the as-designed and as-built simulations. Note the subtle differences on the as-built section (bottom right) beginning at the two-o'clock position and extending to the four-o'clock position. The elevation cross-sections are shown overlaid onto the pressure time plots for visualizing the phantom material boundaries.

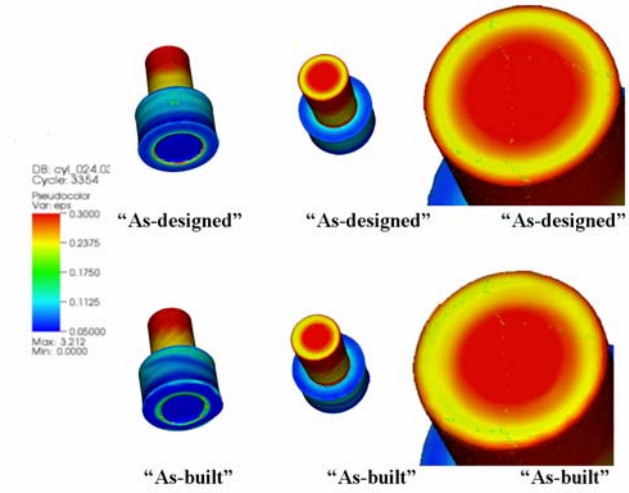

Figure 22: Effective plastic-strain (a useful cumulative state variable) at the final time-state. Again, note the subtle differences (right).

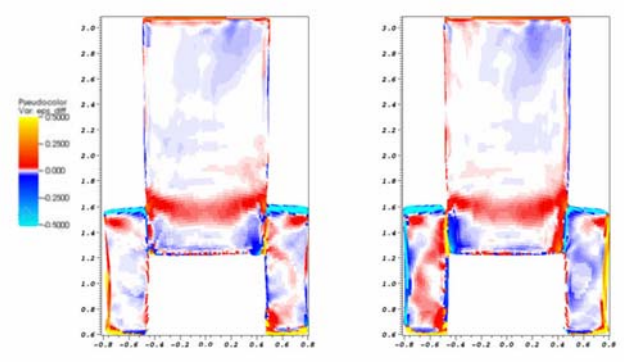

Figure 23: As-designed configuration differenced with as-built configuration. Plot of effective plastic-strain (a useful cumulative state variable) at the final time-state for two orthogonal axial slice planes. Red to yellow regions indicate locations where the as-built configuration accumulated more plastic strain (represented as a percentage ranging from 0.0% to 50.0%) relative to the as-designed configuration. Blue to cyan regions indicate locations where the as-designed configuration accumulated more plastic strain (0.0% to 50.0%) relative to the as-built configuration.

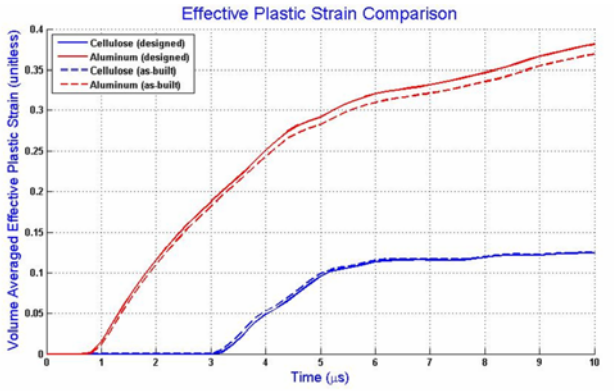

Figure 24: Volume averaged effective plastic strain (a useful cumulative state variable) time-history plot for the as-designed and as-built configurations.

5 Future Work

It is clear from the results of the model simulations that the as-built modeling framework, which incorporates information obtained non-destructively directly into physics and engineering analysis simulations, can provide valuable information to help better understand complex systems. Although useful, the framework has several areas that have room for improvement. In particular, quantifying the error accumulated in both manipulating the data and visualizing large multi-modal data sets, extracting geometric features of interest in a semi-automated fashion, the fusion of multi-modal NDC data sets, and steps through the analysis model mesh generation the initial simulation code assumptions and approximations. At each of these steps, the modified material and geometry information accumulates some measurable variance or error with respect the actual physical part and load case reality. This is currently one of the cruxes of the process.

5.1 Variance / Error Estimation

Currently there is no established methodology for quantifying error accumulated after each operation within the as-built modeling framework. At each step in the process, from the data acquisition step through to the generation of an analysis discretization (or mesh), data sets are manipulated and variation (or error) is accumulated throughout the process of generating the as-built model in both the geometry and material information. Quantifying the error at each step can provide an analyst with a metric of how the initial conditions to the numerical simulation compare to reality. Information gleaned from this exercise would provide useful feedback into the process and may help to define NDC acquisition requirements for future objects of interest and parametric bounds for image processing operations.

5.1.1 Cramer-Rao Bounds

The basic problem in generating as-built models is extracting geometric information of the as-built configuration from NDC data. This can be cast as a classical statistical problem in parameter estimation. The variances of the geometric parameters measure the degree of uncertainty in the as-built configuration. Determining the uncertainty is critical to building a useful as-built model for performance prediction. If the difference between the as-built and as-designed configurations is less than the uncertainty in the as-built model there is little to be gained in using the as-built configuration. Calculating the variances of the geometric parameters for the as-built model is a difficult problem. The most direct way would be to perform the extraction of the geometric parameters from the NDC data many times, then estimating the variances of the parameters over the ensemble of results (Monte-Carlo method). Though statistically accurate, this method would be impractical for most applications. An alternative is to estimate the Cramer-Rao lower bounds of the variances using a result from classical estimation theory [32].

Examples where this approach is used include where the geometric parameter was the object location [33] and where shape information is estimated [34]. These efforts used simulated data to determine the theoretical performance of parametric shape models in extracting information from NDC data. Recently, we compared voxel reconstruction and geometric model-based reconstruction methods using measured data from a simple cylindrical object [35]. Cramer-Rao lower bounds of the parameter variances were calculated from estimates of measurement error. Future work using more complicated objects, relevant to actual applications, is being planned.

5.1.2 VisIt Tool

If VisIt's data analysis capabilities were expanded, it could become an even more powerful diagnostic tool for differencing as-built and as-designed data sets in the future. Currently, the tool can import both types of data and quantify certain analysis metrics such as component centroid, moment of inertia, and volume overlap agreement. In addition, differences in simulation state variable results can be quantitatively explored using recently implemented database comparison expression operators. But certain powerful capabilities are still missing, for example the ability to geometrically auto-register databases and topologically quantify differences between models. Another future improvement includes the import capability for other NDC modalities (such as UT data). Once these features are available, VisIt will be able to generate more complete quantitative reports detailing differences between as-built and as-designed data sets.

5.2 Geometric Parameter Extraction

As mentioned previously, the basic problem of extracting geometric information about the as-built configuration from NDC data can be cast as a classical parameter estimation problem. This approach would be especially appropriate for structured objects like the concentric-cylindrical phantom in Figure 5. For example, if we wished to describe Slice-A of the phantom (see Figure 14), we would need only the two radii and two center coordinates of the epoxy-aluminum interfaces (six parameters). For Slice-B, we add the interface between the epoxy and cellulose for a total of nine parameters. Using these parameters and a model of the physics of X-ray propagation through the materials, we can create simulated sinograms for each slice. Similarly, using an acoustic propagation code we could create simulated ultrasonic sinograms. By comparing these simulated sinograms with the actual sinograms (Figure 12 and 13), we can estimate the value of each geometric parameter. Estimates could be calculated for each data set (X-ray and ultrasonic) individually, or a single set of estimates obtained by combining X-ray and ultrasonic data sets (data fusion). This basic approach lends itself well to data fusion, avoiding many difficulties, such as data registration, that plague other approaches. An example of model-based fusion of electrical resistance and ultrasonic tomographic data can be found in the paper by West and Williams [36].

In addition to data fusion, another advantage of the geometric parameterization approach is that it gives estimates of the uncertainty in the parameters (see previous section on Cramer-Rao Bounds). One disadvantage of the geometric parameterization approach is that it could miss important features that are not incorporated into the object model. Cracks, voids, delaminations, and other defects that could be important to performance may not be detectable unless they are included explicitly in the geometric object model at the beginning. This difficulty with parameterized object models might be reduced by careful comparisons between parameterized reconstructions and conventional, voxel-based reconstructions of NDC data. Large differences could be used to "adapt" the parameterization to capture more features. Another disadvantage of the parameterized object approach is that the data typically depends nonlinearly on the parameters. Thus the whole estimation problem is nonlinear, compared with the usually linear (though often ill-posed) problem of conventional reconstruction. The additional mathematical complication is the price one pays for the advantages of the geometric parameter approach. This is the primary reason why parameterized approaches are not widely used for generating as-built models. However, the potential advantages of the geometric parameter extraction approach provides a strong motivation for solving the mathematical and implementation problems in making it a practical tool for as-built model generation.

6 Summary

This work presents a comparison of simulations for as-built and as-designed models of a cylindrical, multi-material test object. The as-designed model, derived from CAD drawings of the object, and the as-built model, derived from three-dimensional NDE x-ray and ultrasonic data, contain hexahedral finite-

elements. In the simulation, a sharp pressure load was applied uniformly to the top of the cylinder in each model. Comparison of the as-built to the as-designed simulations showed up to 10% local effective plastic strain accumulation differences.

The example presented illustrates our current process for generating an as-built analysis model for predicting performance. While as-designed simulations are good for assessing the design of an object, as-built simulations offer predictive insight into the performance of an object relative to the intended design. The additional effort associated with acquiring better simulation initial conditions (geometry / material) can prove to reduce simulation uncertainty and can be readily justified for high-value parts.

7 Acknowledgements

We thank Earl Updike for helping in the X-ray CT data acquisition, and Paul Souza for helping in the UT data acquisition. We also would like to thank George Albrecht, Rich Becker, and Robert Sharpe for helpful suggestions and continued support for this effort. This work was performed under the auspices of the U.S. Department of Energy by University of California, Lawrence Livermore National Laboratory under Contract W-7405-Eng-48.

8 Disclaimer

9 References

[1] Waters, A.M., Martz, H.E., Dolan, K.W., Horstemeyer, M.F., and Green, R.E., 2000, "Three Dimensional Void Analysis of AM60B Magnesium Alloy Tensile Bars Using Computed Tomography Imagery," *Mat. Eval.*, 58, pp. 1221-1227.

[2] Horstemeyer, M. F., Gall, K., Dolan, K.W., Waters, A., Haskins, J.J., Perkins, D.E., Gokhale, A.M., and Dighe, M.D., 2003, "Numerical, Experimental, Nonedestructive, and Image Analyses of Damage Progression in Cast A356 Aluminum Notch Tensile Bars," *Theoretical and Applied Fracture Mechanics*, 39, pp. 23-45.

[3] Georgeson, G., Crews, A., and Bossi, R., 1992, "X-Ray Computed Tomography Analysis for Concurrent Engineering," *Concurrent Engineering Approach to Materials Processing*, pp. 231-245.

[4] Abd El-Ghany, K.M., and Farag, M.M., 2000, "Expert System to Automate the Finite Element Analysis for Non-Destructive Testing," *NDT&E International*, 33, pp. 409-415.

[5] Balazs, B., Maxwell, R., Kokko, E., DeTeresa, S., and Smith, T., 2002, "Techniques for the Analysis of Aging Signatures of Silica-Filled Siloxanes," *3rd MODEST Conference*, Budapest Hungary.

[6] Boyd, S.K., and Muller, R., 2006, "Smooth surface meshing for automated finite element model generation from 3D image data," *Journal of Biomechanics*, 39(7), pp. 1287-1295.

[7] Hirota, N., and Yoshikawa, N., 2001, "Finite Element Modeling of Textile Composite Using X-ray CT Images," *Proceedings of APCFS & ATEM*, 2, pp. 623-626.

[8] Benko, P., Martin, R., and Varady, T., 2001, "Algorithms for Reverse Engineering Boundary Representation Models," *Computer Aided Design*, 33(11).

[9] Browne, J., Koshy, M., and Stanley, J., 1998, "On the Application of Discrete Tomography to CT-Assisted Engineering and Design," *International Journal of Imaging Systems Technology*, 9.

[10] Menegazzi, P., and Trapy, J., 1997, "A New Approach to the Modelling of Engine Cooling Systems," *Oil & Gas Science and Technology*

(Revue de l'Institut Francais du Petrole), 52(5), pp. 531-539.

[11] Viceconti, M., Davinelli, M., Taddei, F., and Cappello, A., 2004, "Automatic generation of accurate subject-specific bone finite element models to be used in clinical studies," *Journal of Biomechanics*, 37, pp. 1597-1605.

[12] Bossart, P-L, Martz, H.E., Brand, H.R., Hollerbach, K., 1996, "Application of 3D X-ray CT Data Sets to Finite Element Analysis," Review of progress in Quantitative Nondestructive Evaluation, D.O. Thompson and D.E. Chimenti, Eds., Plenum Press, New York, 15, pp. 489-496.

[13] Zhang, Y., and Bajaj, C., 2004, "Adaptive and Quality Quadrilateral / Hexahedral Meshing from Volumetric Data," *13th International Meshing Roundtable, Williamsburg Virginia, USA.*

[14] Zhang, Y., Bajaj, C., and Shon, B.S., 2004, "3D Finite Element Meshing from Imaging Data," *Special Issue of Computer Methods in Applied Mechanics and Engineering on Unstructured Mesh Generation*.

[15] Schmitt, J., Meiforth, J., and Lengsfeld, M., 2001, "Development of a hybrid finite element model for individual simulation of intertrochanteric osteotomies,", *Medical Engineering & Physics*, 23, pp. 529-539.

[16] Stolken, J. S., and Kinney, J.H., 2003, "On the Importance of Geometric Nonlinearity in Finite-Element Simulations of Trabecular Bone Failure," *Bone*, 33, pp. 494-504.

[17] Jaecques, S.V.N, Ooserwyck, H., Mararu, L., Cleynenbreugel, T., Smet, E., Wevers, M., Naert, I., and Vander Sloten, J., 2004, "Individualized, micro CT-based finite element modeling as a tool for biomechanical analysis related to tissue engineering of bone," *Biomaterials*, 25, pp. 1683-1696.

[18] Taylor, C., Hughes, T., and Zarins, C., 1998, "Finite Element Modeling of Blood Flow in Arteries," *Computational Methods in Applied Mechanics and Engineering*, 158, pp 155-196.

[19] Antiga, L., Ene-Iordache, B., Caverni, L., Cornalba, G.P., and Remuzzi, A., 2002, "Geometric Reconstruction for Computational Mesh Generation of Arterial Bifurcations from CT Angiography," *Computerized Medical Imaging and Graphics*, 26, pp. 227-235.

[20] Wu Z., and Sullivan, J., 2001, "Automatic Finite Element Mesh Generation from MRI Scans for Breast Cancer Investigations," *Proceedings of the IEEE 27th Annual Northeast Bioengineering Conference*.

[21] Barrett, H.H., and Swindell, W., 1981, Radiological Imaging, Academic Press, New York.

[22] Martz, H.E., Jr., Logan, C.M., and Shull, P.J., 2002, "Radiology", Nondestructive Evaluation: Theory, Techniques and Applications, Peter J. Shull, Ed Marcel Dekker, Inc., New York, NY.

[23] Chawner, J., 2003, "Issues in Applied Mesh Generation", Pre-Conference Short Course: Mesh Generation and Automated Simulation," *7th National Congress on Computational Mechanics*.

[24] Childs, H., Brugger, E., Bonnell, K., Meredith, J., Miller, M., Whitlock, B., and Max, N., 2005, "A Contract Based System for Large Data Visualization," *Proceedings of IEEE Visualization*.

[25] TrueGrid Manual, 2000, Version 2.0.0 Revision 2., XYZ Scientific Applications, Inc..

[26] Cubit On-Line Manual, 2005, Version 10.0., Sandia National Laboratories.

[27] Sheffer, A., and Bercovier, M., 2000, "Hexahedral Meshing of Non-Linear Volumes Using Voronoi Faces and Edges," *International Journal of Numerical Methods in Engineering*, 49.

[28] Bern, M., and Plassmann, P., 1999, "Mesh Generation," Handbook of Computational Geometry, 6.

[29] Owen, S., 2003, "An Introduction to Unstructured Mesh Generation," *Pre-Conference Short Course: Mesh Generation and Automated Simulation, 7th National Congress on Computational Mechanics*.

[30] Garimella, R.,2003, "Untangling of 2D Triangular and Quadrilateral Meshes in ALE Simulations," *Workshop on Mesh Quality and Dynamic Meshing, 7th National Congress on Computational Mechanics*.

[31] Sharp, R., et. al., 2005, "Users Manual for ALE3D: An Arbitrary Lagrange/Eulerian 3D Code System,", UCRL-MA-152204 Rev. 3.

[32] H. L. Van Trees, 1968, “Detection, Estimation, and Modulation Theory, Part I,” John Wiley & Sons.

[33] D. J. Rossi and Wilsky, A.S., 1984, “Reconstruction from projections based on detection and estimation of objects – Parts I and II: Performance analysis and robustness analysis,” *IEEE Trans. Acoust. Speech, Signal Proc.*, ASSP-32, pp. 886-906.

[34] Ye, J.C., Bressler, Y., and Moulin, P., 2003, “Cramer-Rao bounds for parametric shape estimation in inverse problems,” *IEEE Trans. Image Proc.*, Vol. 12, pp. 71-84, 2003.

[35] Chambers, D. H., Goodman, D.M., and Leach, R.R., 2003, “As-Built Model Generation for a Cylindrical Test Object,” Lawrence Livermore National Laboratory, UCRL-TR-200695.

[36] West, R.W., and Williams, R.A., 1999, “Opportunities for data fusion in multi-modality tomography,” *1st World Congress Industrial Process Tomography*, pp. 195-200.